Received: 30 October 2023 | Revised: 24 January 2024 | Accepted: 2 February 2024

DOI: 10.1002/trc2.12459

Alzheimer's & Dementia
Translational Research & Clinical Interventions

RESEARCH ARTICLE

Distribution of insulin in primate brain following nose-to-brain transport

Kylie Smith[1,2] | Jinda Fan[2,3,4] | Gwendolyn A. Marriner[5] | John Gerdes[6] | Robert Kessler[4] | Kurt R. Zinn[1,2,4,7]

[1]Department of Biomedical Engineering, Michigan State University, East Lansing, Michigan, USA

[2]Institute for Quantitative Health Science and Engineering, Michigan State University, East Lansing, Michigan, USA

[3]Department of Chemistry, Michigan State University, East Lansing, Michigan, USA

[4]Department of Radiology, Michigan State University, East Lansing, Michigan, USA

[5]Department of Molecular Imaging, Charles River Laboratories, Mattawan, Michigan, USA

[6]Department of Biomedical and Pharmaceutical Sciences, University of Montana, Missoula, Montana, USA

[7]Department of Small Animal Clinical Sciences, Michigan State University, East Lansing, Michigan, USA

Correspondence
Kurt R. Zinn, Departments of Radiology, Biomedical Engineering, Small Animal Clinical Sciences, Michigan State University, East Lansing, MI, USA.
Email: zinnkurt@msu.edu

Funding information
National Institutes of Health, Grant/Award Number: R21AG054960

Abstract

Introduction: Nose-to-brain (N2B) insulin delivery has potential for Alzheimer's disease (AD) therapy. However, clinical implementation has been challenging without methods to follow N2B delivery non-invasively. Positron emission tomography (PET) was applied to measure F-18-labeled insulin ([^{18}F]FB-insulin) from intranasal dosing to brain uptake in non-human primates following N2B delivery.

Methods: [^{18}F]FB-insulin was prepared by reacting A^{1},B^{29}-di(tert-butyloxy carbonyl)insulin with [^{18}F]-*N*-succinimidyl-4-fluorobenzoate. Three methods of N2B delivery for [^{18}F]FB-insulin were compared – delivery as aerosol via tubing (rhesus macaque, $n = 2$), as aerosol via preplaced catheter (rhesus macaque, $n = 3$), and as solution via preplaced catheter (cynomolgus macaque, $n = 3$). Following dosing, dynamic PET imaging (120 min) quantified delivery efficiency to the nasal cavity and whole brain. Area under the time-activity curve was calculated for 46 regions of the cynomolgus macaque brain to determine regional [^{18}F]FB-insulin levels.

Results: Liquid instillation of [^{18}F]FB-insulin by catheter outperformed aerosol methods for delivery to the subject (39.89% injected dose vs 10.03% for aerosol via tubing, 0.17% for aerosol by catheter) and subsequently to brain (0.34% injected dose vs 0.00020% for aerosol via tubing, 0.05% for aerosol by catheter). [^{18}F]FB-insulin was rapidly transferred across the cribriform plate to limbic and frontotemporal areas responsible for emotional and memory processing. [^{18}F]FB-insulin half-life was longer in olfactory nerve projection sites with high insulin receptor density compared to the whole brain.

Discussion: The catheter-based liquid delivery approach combined with PET imaging successfully tracked the fate of N2B [^{18}F]FB-insulin and is thought to be broadly applicable for assessments of other therapeutic agents. This method can be rapidly applied in humans to advance clinical evaluation of N2B insulin as an AD therapeutic.

KEYWORDS
Alzheimer's disease, cranial nerves, cribriform plate, dementia, dynamic imaging, image-guided delivery, intervention, intranasal insulin, neuroprotection, non-invasive imaging, positron emission tomography (PET)

Highlights for

- [^{18}F]FB-insulin passage across the cribriform plate was detected by PET.
- Intranasal [^{18}F]FB-insulin reached the brain within 13 min.
- [^{18}F]FB-insulin activity was highest in emotional and memory processing regions.
- Aerosol delivery was less efficient than liquid instillation by preplaced catheter.
- Insulin delivery to the cribriform plate was critical for arrival in the brain.

1 | INTRODUCTION

Restoration of insulin levels in the central nervous system (CNS) has gained attention as a prospective therapy for Alzheimer's disease (AD). AD patients have higher plasma and lower cerebrospinal fluid (CSF) insulin levels in a pattern that intensifies with the severity of their clinical impairment.[1] This is exacerbated by reports of lower insulin receptor (IR) levels in regions responsible for higher-order cognition[2] and altered IR isoform expression at the blood–brain barrier (BBB) compared to healthy controls.[3] Supplementing CNS insulin levels has been found to improve performance on memory tasks,[4–8] mood,[9,10] and cerebral metabolism in key processing areas.[6,11] However, this approach is challenged by the need to maintain tightly regulated peripheral insulin homeostasis. Early efforts employed a euglycemic clamp to raise plasma insulin levels while maintaining plasma glucose at a fasting baseline,[8] but the technical complexity of this method limits its application for routine patient use. An alternate route of insulin delivery to the CNS that avoids systemic circulation is needed.

N2B delivery of insulin has gained attention as a route to non-invasively improve CSF insulin levels without perturbing peripheral insulin levels. Rodent studies suggest that molecules delivered N2B travel along olfactory (CN I) and trigeminal (CN V) nerves to reach the CNS instead of relying on the circulatory system.[12–15] Thus, N2B therapeutics avoid the restrictive BBB, undesirable off-target effects, and hepatic metabolism.[16–18] Drug delivery via this route is reported to improve patient compliance[19] and occur quickly,[12,20] evidenced by a doubling of CSF insulin levels within 30 min of a 40 IU dose of intranasal insulin.[21] As an AD treatment, N2B insulin improved recall performance,[7] improved capacity for self-care, and preserved performance on the cognitive subscale of the Alzheimer's Disease Assessment Scale (ADAS-cog).[6] These improvements correlated with glucose utilization and arrest of atrophy in characteristic AD hypometabolic regions as determined by [ź^{8}F]fluorodeoxyglucose positron emission tomography (PET)[6] and magnetic resonance imaging (MRI).[22] Perhaps most importantly, after improved cognition, cell culture studies suggest that insulin protects neurons from damage induced by amyloid beta (Aβ) and phosphorylated tau, the pathophysiological hallmarks of AD, via IR engagement and downstream signaling.[23,24] Inspired by the demonstrated safety profile and benefits of N2B insulin on attention, memory, and higher-order cognitive functions in patients with early AD,[4,6,7,16,22,25–30] the National Institutes of Health has awarded substantial funding for the development of N2B insulin as an AD treatment.[26]

Efforts to demonstrate the clinical efficacy of N2B insulin as an AD treatment have yielded inconclusive results. The most notable example comes from the Phase 2/3 clinical trial published by Suzanne Craft and others in 2020.[30] This study was intended to investigate the safety and efficacy of N2B insulin treatment for patients with AD or MCI over 12 months. Although the trial methodology originally mirrored earlier studies that demonstrated improved recall and cognitive preservation (ADAS-cog and Activities of Daily Living scale)[6,7,22] following N2B insulin treatment, a change in delivery device was needed midway through the trial due to inconsistent device performance. Primary trial outcomes were derived from the patient group receiving insulin via the newer device (Impel NeuroPharma's Precision Olfactory Delivery device, $n = 240$), which indicated no benefit from N2B insulin on cognitive tests (four administered), CSF biomarkers (four tested), or cortical preservation from atrophy. However, subjects that received insulin via the original device (Kurve Technology's ViaNase nebulizer, $n = 42$), which had been previously validated by the same researchers, showed modest improvements in Aβ clearance, improved performance on cognitive tests, and preserved hippocampal volume.[30] It is unclear whether the lack of treatment effect observed in the primary cohort was a consequence of administration device design or technique,[31] lack of efficacy of intranasal insulin, or something else. This study highlights the need to verify a device's "ability to deliver compounds to the central nervous system directly."[30] There is no way to eliminate device performance as a potential source of treatment failure without a method to validate transfer of drug from the device to the target site. However, tracking the distribution of small volumes through the narrow, bony structures of the skull is challenging in living subjects.

A non-invasive method to track the deposition and transfer of N2B therapeutics in living subjects is needed. We hypothesized that N2B [^{18}F]FB-insulin would reach the brain via transfer across the cribriform plate and be detectable by PET, resulting in differentially elevated levels of insulin in cerebrospinal fluid and nervous tissue. We tested three N2B delivery approaches in macaques, comprising specific and non-specific methods for radiotracer delivery to the upper nasal cavity as solution or aerosol, respectively. CNS [^{18}F]FB-insulin levels were regionally quantified using a species-specific brain atlas applied to

co-registered PET, computed tomography (CT), and magnetic resonance (MR) images. This work was expected to outline a translatable PET imaging platform to rigorously assess [^{18}F]FB-insulin distribution in the CNS over time and enable identification of prevailing interventions for AD patients.

2 | METHODS

2.1 | Synthesis of [^{18}F]FB-insulin

[^{18}F]FB-insulin was synthesized at Charles River Laboratories (Mattawan, MI, USA) by reacting [^{18}F]-succinimidyl-fluorobenzoate ([^{18}F]-SFB) produced on site with A^{1},B^{29}-di(*tert*-butyloxycarbonyl)insulin (di(Boc)insulin) prepared at Michigan State University (see Figure A.1A in supporting information Appendix A). Chemical and radiochemical purities/identities were analyzed using high-performance liquid chromatography (HPLC) equipped with sequential ultraviolet (UV) spectroscopy and radiation detectors. Identity was confirmed by comparing the retention time (R_t) of the radiolabeled product with that of the corresponding unlabeled reference standard (see Figure A.1B-D in supporting information Appendix A). For dosing, the product was diluted with saline to reach the desired volume with <10% ethanol/saline V/V.

2.2 | [^{18}F]FB-insulin delivery to subjects

[^{18}F]FB-insulin was delivered to anesthetized (10 mg/kg intramuscular ketamine, isoflurane to effect) rhesus macaques (one male, one female) as aerosol or cynomolgus macaques (one male, one female) as liquid (Figure 1). The change to cynomolgus, which have a nasal cavity architecture similar to that of rhesus, was required due to pandemic-related supply chain issues. For the former, [^{18}F]FB-insulin was aerosolized using an enclosed vibrating mesh nebulizer and delivered to subjects via Tygon tubing (non-specific delivery to target site, $n = 2$) or catheter (specific delivery to target site, $n = 3$). For the latter, [^{18}F]FB-insulin was delivered to the upper nasal cavity of subjects in liquid form ($n = 3$) by attaching the free end of the catheter to a dose-filled syringe that delivered 450 µL of [^{18}F]FB-insulin by syringe pump (4-min duration at 7.5 mL/h). Subjects were positioned prone for catheter-based delivery methods per surgeon recommendations and were supine otherwise. Additional details regarding aerosol dosing can be found in Section 2.2 of supporting information Appendix A. Subject and dose summaries are given in Table B.2 of supporting information Appendix B.

All procedures involving animal subjects were approved by the Charles River Laboratories Institutional Animal Care and Use Committee and were conducted in compliance with the Public Health Service Policy on Humane Care and Use of Laboratory Animals from the Office of Laboratory Animal Welfare and the Guide for the Care and Use of Laboratory Animals from the National Research Council. Subjects were consistently monitored while under anesthesia (vitals reported in Figure B.1 of supporting information Appendix B).

RESEARCH IN CONTEXT

1. **Systematic review**: The phrases "intranasal insulin," "IN insulin," "nose-to-brain insulin," "nose-to-brain insulin," and "N2B insulin" were searched on Google Scholar and Michigan State University Library's catalog to identify existing publications.
2. **Interpretation**: This research demonstrated the first clinically viable method to dynamically image N2B insulin transfer. The transport of [^{18}F]FB-insulin across the cribriform plate was important for brain uptake, seen significantly less with aerosol than liquid. Frontotemporal cortices vulnerable to neurodegeneration in Alzheimer's disease were [^{18}F]FB-insulin accumulation sites for this pathway.
3. **Future directions**: Future work should compare PET imaging results with additional measurements of [^{18}F]FB-insulin and metabolites in plasma and cerebrospinal fluid samples. Additionally, a study that demonstrates the cognitive benefits of N2B insulin with [^{18}F]FB-insulin incorporated into the therapeutic dose would be useful if followed by imaging, with and without insulin receptor blocking, to validate the involvement of target sites.

2.3 | Image acquisition and analysis

For all methods, subjects were transferred to the PET scanner (MicroPET Focus 220, Siemens) immediately following dosing for a 120-min head-focused dynamic acquisition. A CT scan followed PET imaging to facilitate image corrections and registration. A MR image was acquired on a separate day for anatomical reference. PET, CT, and MR images were co-registered and resampled to a uniform voxel size (0.6 mm^3) for regional analysis in VivoQuant (inviCRO). [^{18}F]FB-insulin remaining on dosing accessories was quantified by dose calibrator or PET scanner (MicroPET Focus 120) and used to calculate the injected dose (%ID) by subtracting the starting dose from the summed residual activity.

For all delivery conditions, deposition fractions were calculated for delivery components leading to and including the subject as percentage of the starting dose (%SD). [^{18}F]FB-insulin in the nasal cavity, cribriform plate, whole brain, and field of view (FOV) was quantified as %ID using static PET reconstructions. For dynamic images acquired following liquid radiotracer delivery, time-activity curves (TACs) were generated for the nasal cavity, cribriform plate, whole brain, and brain atlas regions (see Figure A.3 in supporting information Appendix A) using species-specific MR-based atlases provided by inviCRO. Mean and standard error of the mean (SEM) were calculated for each time point and atlas region ($n = 46$) as %ID, %ID/mm^3, standard uptake value (SUV, g/mm^3), and SUV relative to the whole brain (nSUV). Area under the curve (AUC) was calculated via the trapezoidal method for

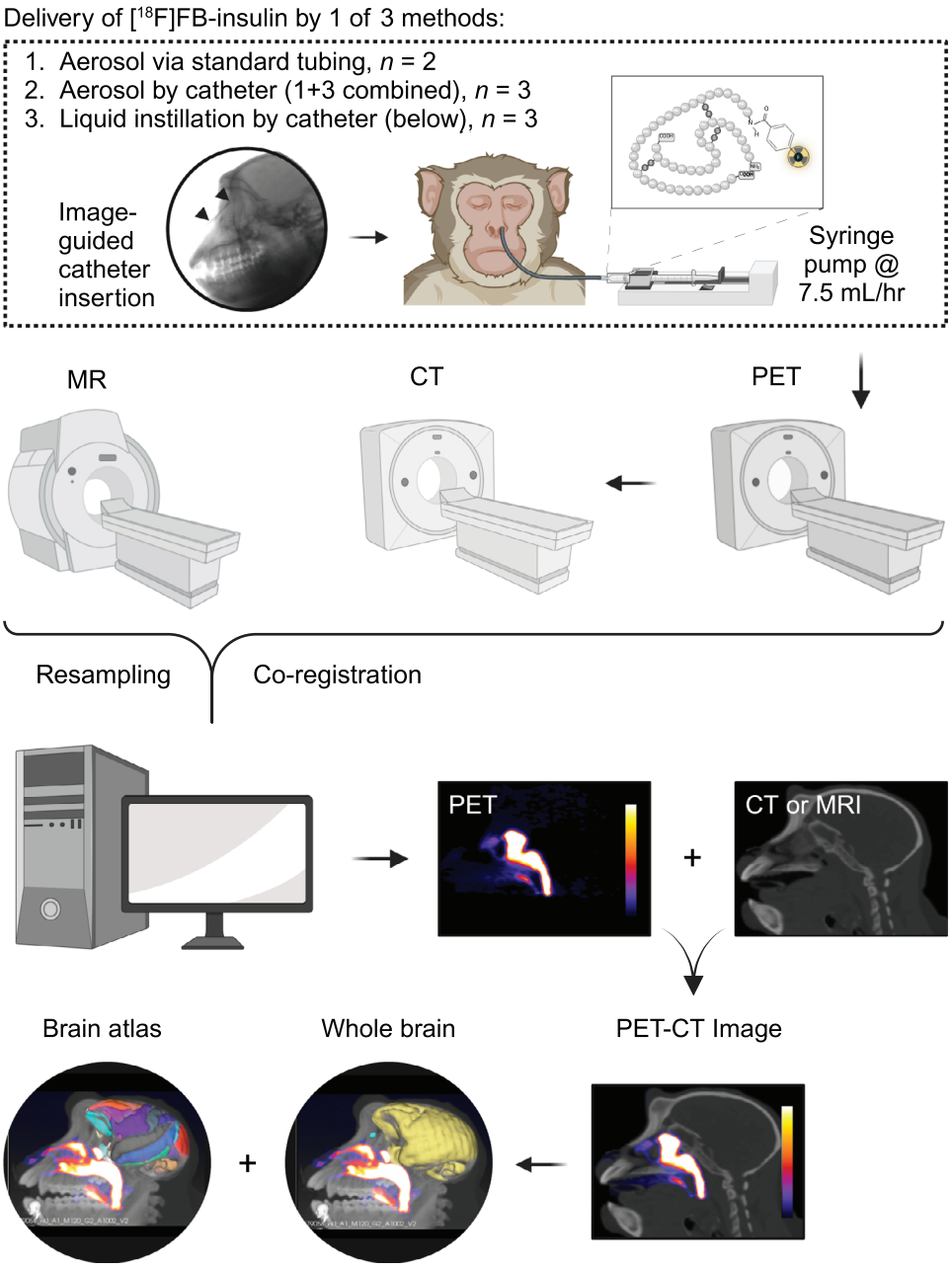

FIGURE 1 Workflow for [18F]FB-insulin dosing and imaging by dynamic PET, CT, and MR in rhesus and cynomolgus macaques. Radiotracer was delivered in aerosol (rhesus macaques, $n = 2$ via tubing, $n = 3$ via catheter) or liquid (cynomolgus macaques, $n = 3$) form prior to 120 min of dynamic PET imaging, followed by CT. PET, CT, and MR images (MR acquired separately) were resampled to uniform voxel size and co-registered for analysis. A fluoroscope was used to place the catheter used in delivery methods 2 and 3, which is visible between the black arrowheads in the top left. Example cribriform plate (green), whole brain (yellow), and brain atlas (multicolored) volumes of interest are shown in the bottom row. Atlas quantification was performed only in subjects receiving liquid dosing by catheter. CT, computed tomography; MR, magnetic resonance; PET, positron emission tomography.

regional SUV TACs and compared via Tukey's test in GraphPad Prism (GraphPad, LLC). A one-phase exponential decay model was applied to individual TACs to estimate regional clearance kinetics for [18F]FB-insulin following peak brain uptake ($T > 27$ min after dose, fixed parameters: $K > 0$, plateau > 0) in the same program. Full image acquisition and analysis methods are reported in supporting information Appendix A.

3 | RESULTS

3.1 | Radiochemistry

[18F]FB-insulin was synthesized with 99.97% (± 0.030 SEM) radiochemical purity within 81 min (± 2.77 SEM) on average, achieving a decay-corrected radiochemical yield of 11.5% (± 2.63 SEM) and

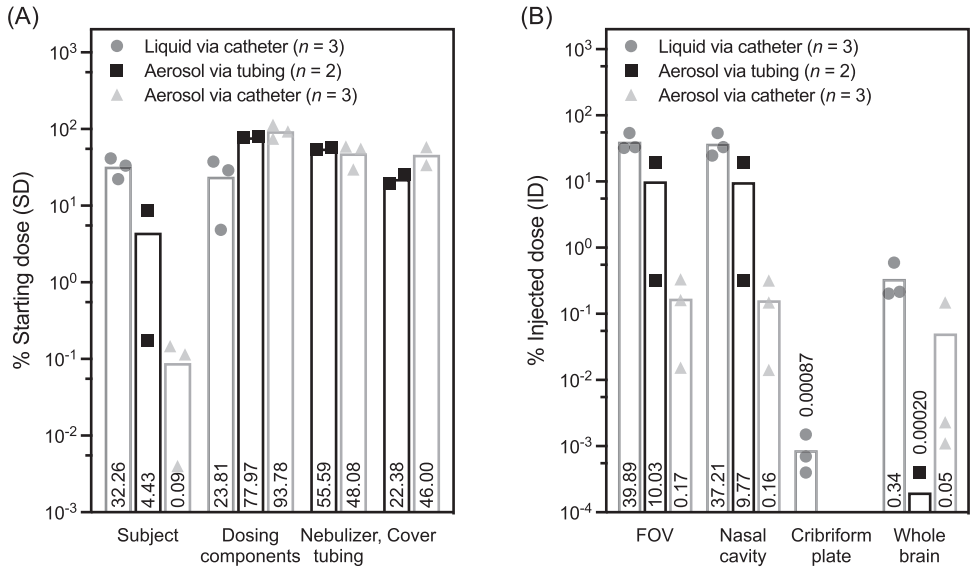

FIGURE 2 [18F]FB-insulin delivery to subject versus components of dosing apparatus. (A) Percentage of [18F]FB-insulin deposited was calculated for each component of the delivery pathway based on starting dose. Residual dose lost to dosing components includes activity from the custom nebulizer cover, nebulizer, and its accessories. (B) Distribution of injected/delivered dose (ID) within static PET FOV. Means are plotted and printed in each bar. FOV, field of view; ID, percentage of injected/delivered dose; PET, positron emission tomography; SD, percentage of starting dose.

specific activity of 2.988 TBq/mmol (± 1.358 SEM, $n = 8$). Starting doses measured 36.77 MBq (± 11.28 SEM, 0.45-0.9 mL) and contained 6.69×10^{-5} mmol insulin (± 2.84×10^{-5} SEM) on average. [18F]FB-insulin synthesis metrics are reported in Tables B.1 (summary of all experiments) and B.3 (individual experiments) in supporting information Appendix B.

3.2 | [18F]FB-insulin deposition by static PET images

Delivery of [18F]FB-insulin solution via catheter was the most efficient of the three methods tested. Low delivery efficiency for aerosol methods is partly a result of the aerosol settling on components of the dosing apparatus, particularly the three-dimensionally printed nebulizer cover (Figure 2). Incorporation of the catheter for aerosol delivery improved the fraction of tracer detected in the brain (0.050% ID ± 0.049 SEM, range 0.0011% to 0.15%) relative to aerosol delivered by tubing (0.00020% ID, range 0 to 0.00040%), but reduced deposition in the subject overall (catheter at 0.087% SD ± 0.043 SEM, range 0.0040% to 0.15% SD vs tubing at 4.43% SD, range 0.17% to 8.70% SD) due to greater tracer loss to impaction in the nebulizer cover. Comprehensive aerosol delivery results are reported in supporting information Appendix B. Direct delivery of [18F]FB-insulin to the upper nasal cavity by liquid instillation minimized dose loss and variability and resulted in the greatest levels of insulin in the brain (0.34% ID ± 0.13 SEM, range 0.20% to 0.59%). Liquid instillation achieved 39.89% ID (± 7.17 SEM, range 32.22% to 54.22%) deposition in the subject and was the only condition that detected radiotracer transfer across the cribriform plate (0.00087% ID ± 0.00036 SEM, range 0.00040% to 0.0015%). These results suggest that the delivery of [18F]FB-insulin to the brain is strongly dependent on the ability of the method used to deliver [18F]FB-insulin to the cribriform plate.

3.3 | [18F]FB-insulin deposition by dynamic PET images

[18F]FB-insulin administered via liquid instillation rapidly and consistently facilitated N2B transfer through the cribriform plate. Quantification of VOIs in the first PET frame ($T = 12.5$ min after dose onset) revealed 71.47% ID (± 15.18 SEM) in the nasal cavity (Figure 3B), accounting for 99.44% of the total signal in the FOV. At the same time, 0.0036% of tracer was detected in the cribriform plate and 0.38% in the brain, accounting for 0.0026% ID (± 0.0021 SEM) and 0.27% ID (± 0.21 SEM), respectively. The mean whole brain TAC peaked at 0.69% ID within 27 min of dose onset (see Figure B.2 in supporting information Appendix B), constituting 0.97% of the dose initially detected in the nasal cavity. Maximum whole brain [18F]FB-insulin concentration occurred in the first PET frame for two of the three experiments, indicating that intranasally delivered insulin reaches the brain within 13 min of dosing. Interestingly, the two scans with C_{max} in the first frame were acquired in the female subject (T_{max} range for all brain regions = 12.5 to 22 min), while the male subject had a much wider T_{max} range (22 to 87 min for all brain regions), with the cribriform plate T_{max} lagging at 87 min after dosing. Further investigation with a larger sample size would be needed to determine whether this is a sex-based difference. Radiotracer distribution in CNS subregions was not characterized for aerosol methods due to the low overall activity in the brain.

Unlike the other [18F]FB-insulin administration methods tested, delivery of tracer in liquid form consistently distributed tracer

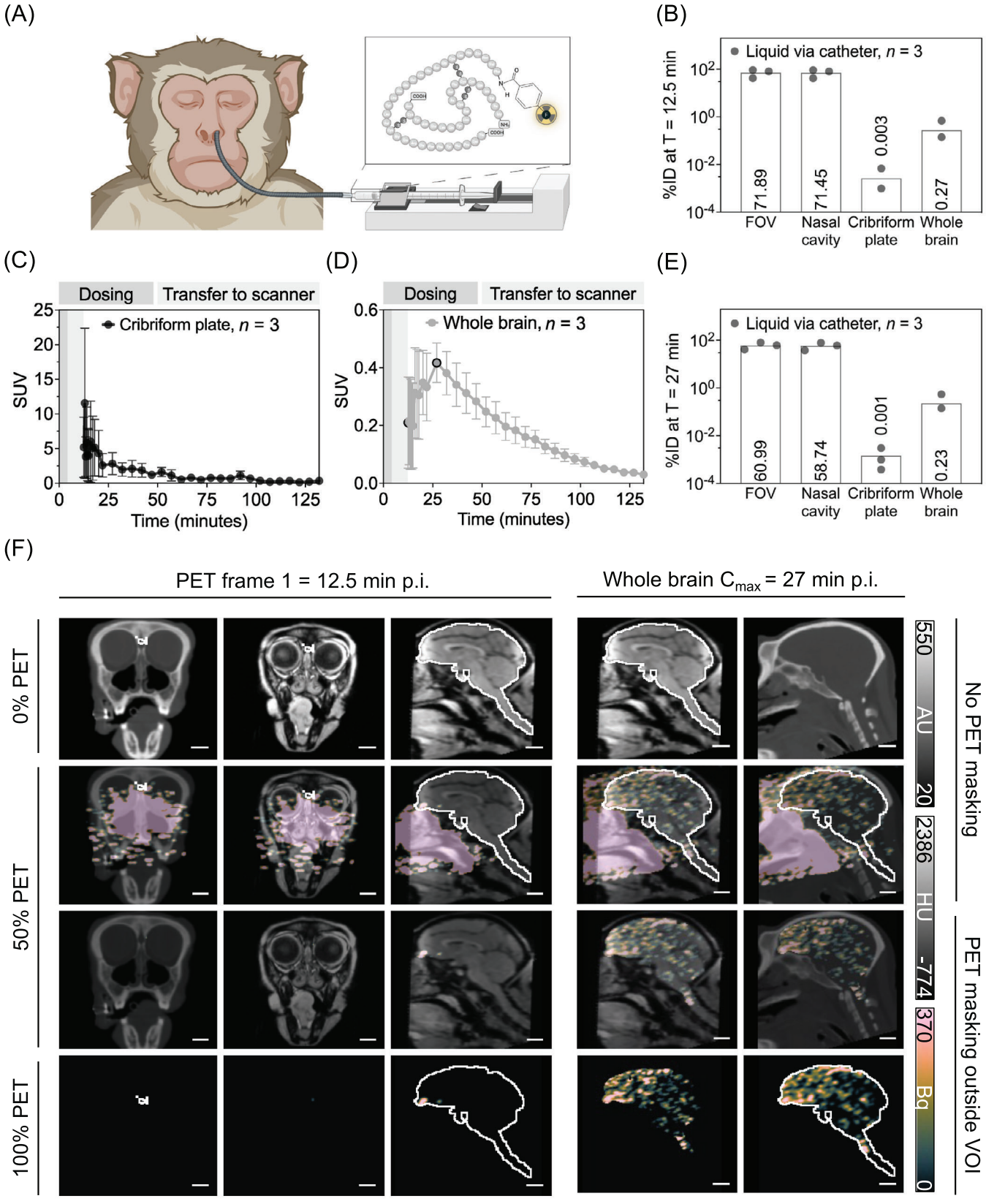

FIGURE 3 [^{18}F]FB-insulin is detected in cribriform plate and brain within 13 min of delivery by catheter. (A and B) The majority of radiotracer delivered via liquid instillation (A, $n = 3$) is retained in the nasal cavity 12.5 min later (B). (C) [^{18}F]FB-insulin transfer across cribriform plate is evident in earliest PET time points. (D) [^{18}F]FB-insulin is present in brain within 12.5 min of dosing and rises to SUV C_{max} by 27 min. (E) Average quantification of [^{18}F]FB-insulin in volumes of interest at $T = 27$ min after dosing when brain uptake is highest per averaged time-activity curve. (F) Co-registered CT (columns 1,5), MR (columns 2-4), and PET (all columns) images shown in coronal and sagittal viewing planes for time points

throughout the nasal cavity, including to the upper nasal cavity, where the olfactory epithelium is located. Tracer was observed primarily within the subject as viewed by CT (Figure 3F), although contamination was visible on the exterior of the head in one of the three subjects. The PET image was dominated by [^{18}F]FB-insulin in the nasal cavity prior to masking outside of the CNS (Figure 3F). Evidence of rapid N2B transmission across the cribriform plate is visible as [^{18}F]FB-insulin signal in the olfactory bulb in early PET frames (Figure 3F).

[^{18}F]FB-insulin accumulation was highest in the limbic lobe, forebrain, and temporal lobe. Within these regions, [^{18}F]FB-insulin exposure to the inferior temporal gyrus and fronto-orbital gyrus was twofold higher than available in the averaged whole brain (Figure 4). Interestingly, the fronto-orbital gyrus had statistically greater bioavailability than the ventricles, which is the primary sampling endpoint for N2B delivery studies in humans and non-human primates. The dentate gyrus, hippocampus, amygdala, nucleus accumbens, and hindbrain also demonstrated high levels of accumulation. If nSUV TACs were used to calculate the AUC instead of the SUV TAC, the top 5 to 10 accumulating regions reshuffle such that the anterior cingulate gyrus occupies a top 10 position (see Figure B.3 in supporting information Appendix B). Top regions for peak concentration (SUV_{max}) but not AUC (eg, subthalamus, archicortex, and subregions of the caudate nucleus) may function as intranasal delivery throughways that material passes through to reach other sites (see Figure B.5 in supporting information Appendix B). Conversely, there was consensus between the regions with the lowest AUC and SUV_{max} values, including the occipital gyrus through the postcentral gyrus regions in Figure 4.

[^{18}F]FB-insulin accumulation and clearance rates varied regionally. A one-phase decay model used to estimate the clearance kinetics of [^{18}F]FB-insulin via averaged regional TACs indicated similar half-lives for the nasal cavity (29.95 min), cribriform plate (20.45 min), and whole brain (30.62 min). The decay model fit the averaged nasal cavity and whole brain TACs well ($R^2 > 0.99$), but less so for the cribriform plate ($R^2 < 0.90$), reflected in a wider confidence interval for the cribriform plate half-life (95% CI 13.12 to 31.45 min). Differences in [^{18}F]FB-insulin kinetics were easily visualized via averaged nSUV TACs for atlas regions (VOI/whole brain, Figure 5). Half-lives estimated by the same approach (R^2 0.62 to 0.99) differentiate regions with high availability of [^{18}F]FB-insulin into high-retention regions or those with kinetics similar to the whole brain. For example, the fronto-orbital gyrus, inferior temporal gyrus, and anterior cingulate cortex demonstrated sustained activity above the whole brain concentration throughout the dynamic PET scan but show steeper SUV clearance slopes than other regions highlighted in Figure 5. Alternatively, the amygdala, hindbrain, hippocampus, and dentate gyrus cleared tracer slower than the whole brain at later time points, demonstrated by their longer half-lives (mean range 40 to 55 min). The oscillating pattern observed for the nucleus accumbens was unique among the other averaged TACs (see Figure B.4 in supporting information Appendix B for heatmap summary of all regions) and was preserved across individual scans (Figure 5).

4 | DISCUSSION

This work demonstrates the feasibility of tracking N2B transfer using existing and clinically relevant neuroimaging tools. PET imaging detected [^{18}F]FB-insulin in the brain following all delivery methods, with the greatest CNS concentration resulting from liquid instillation by catheter. In agreement with our hypothesis, PET informed detailed regional and temporal differences in CNS [^{18}F]FB-insulin concentration, unlike former research that relied on discrete CSF sampling,[20,21] behavioral assays,[32] or *post mortem* tissue analyses[20,33] to draw conclusions following N2B delivery. Limbic and frontotemporal areas were identified as primary accumulation sites for N2B [^{18}F]FB-insulin and not CSF, which is frequently used as a proxy for the concentration of drug in the brain. Limbic and frontotemporal cortical regions are important therapeutic targets for AD patients, as a recent study categorized AD patients primarily into "temporoparietal" or "limbic-predominant" hypometabolic patterns.[34] Further, tau and amyloid aggregations initially appear near the entorhinal cortices and associated sites also known to receive olfactory nerve (CN I) projections such as the amygdala, hippocampus, and parahippocampal regions.[35] N2B insulin delivered via liquid instillation has the potential to address these vulnerabilities in AD through improved cognitive symptoms and/or mitigation of damage induced by tau and Aβ if a similar pattern of distribution is observed following translation of our method to humans, which is an aim of future work. Beyond AD, the N2B route may be promising for the delivery of therapeutics relevant to other injury/disease states with limbic and frontotemporal vulnerability, such as various frontotemporal dementias,[36] global brain ischemia,[37] and more.[38–40]

The amount of insulin needed at the site of action to improve AD and MCI cognitive performance is not currently known. However, differences in CSF insulin concentration for AD patients and healthy controls help to contextualize dosing needs. Given our finding of a 0.010% ID ventricular C_{max} (see Figure B.6 in supporting information Appendix B), a 40 IU starting dose of N2B insulin is estimated to increase CSF insulin levels by 9.34 picomol. Assuming a CSF volume of 0.13 L,[41] this addition

represented in B and E. A CNS VOI generated within intracranial and intravertebral compartments (white outline) was used to improve visibility of [^{18}F]FB-insulin signal in neural tissue by masking PET values outside of VOI to zero. The olfactory bulb and cranial nerves are outlined in columns 1 and 2. [^{18}F]FB-insulin is concentrated in the olfactory bulb in columns 3 to 5. The grayscale AU color bar denotes the range for MR images, the grayscale HU color bar denotes the range for CT images, and the batlowK Bq color map denotes the range for the PET data. Time devoted to dosing or subject transfer to PET scanner is indicated by darker and lighter gray rectangles in plots C and D, respectively. Scale bar = 1 cm. Plots B–E given as mean ± standard error (SEM), with the mean value additionally printed in bars for B and E. Bq, becquerel; C_{max}, maximum concentration; CNS, central nervous system; CT, computed tomography; %ID, percentage of injected/delivered dose; MR, magnetic resonance; PET, positron emission tomography; p.i., post-administration onset; SUV, standard uptake value; VOI, volume of interest.

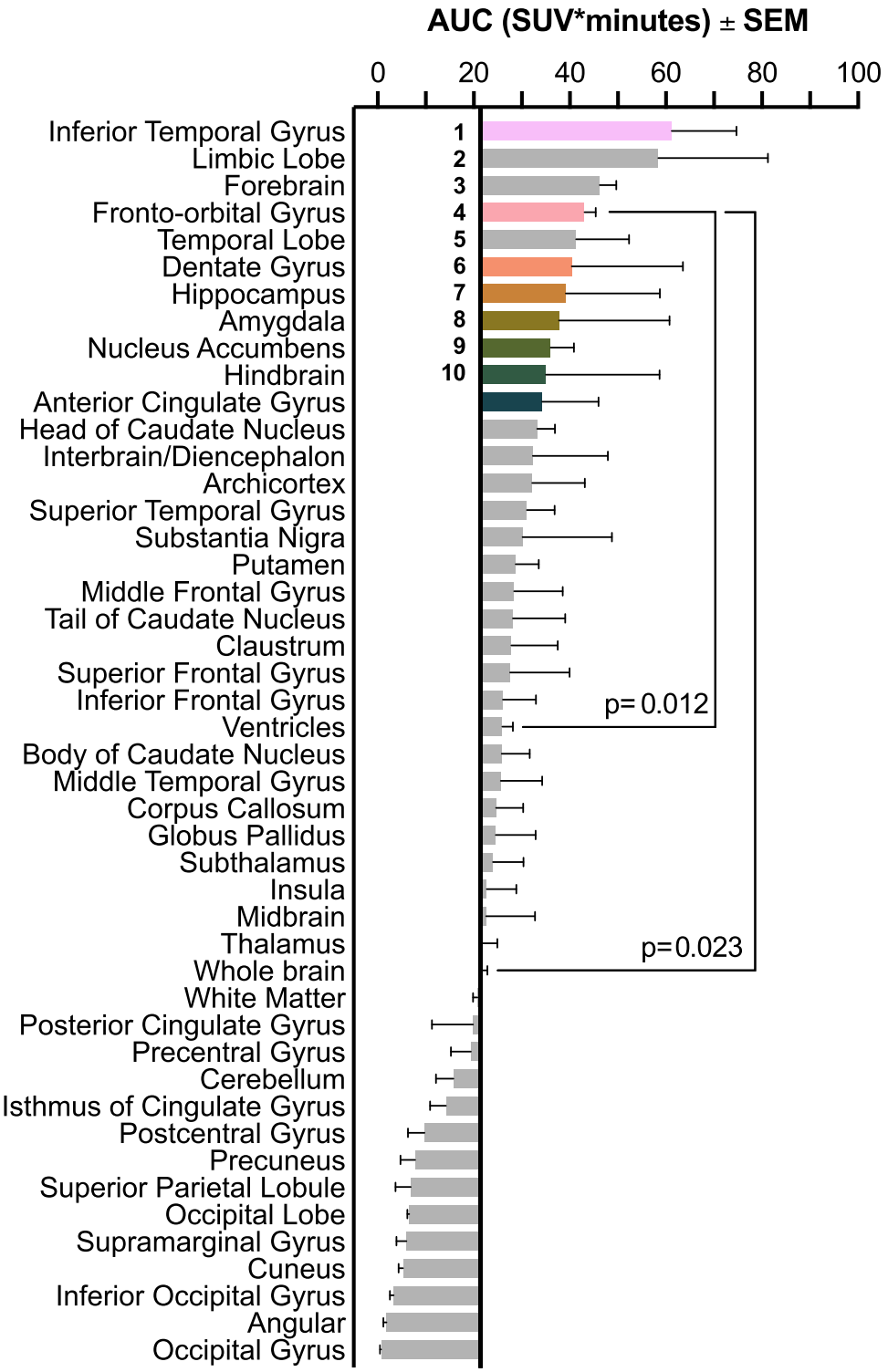

FIGURE 4 [^{18}F]FB-insulin is predominantly found in limbic and frontotemporal cortical regions 120 min following N2B delivery by liquid instillation. Brain atlas regions ranked from highest to lowest accumulation of [^{18}F]FB-insulin according to AUC values (SUV*minutes, $n = 3$) from individual time-activity curves. AUC values are plotted as means ± standard error (SEM). Significant differences determined by Tukey's test. Statistical differences were also found for forebrain and nucleus accumbens but are not highlighted in this plot for clarity. AUC, area under the curve; N2B, nose-to-brain; SEM, standard error of the mean; SUV, standard uptake value.

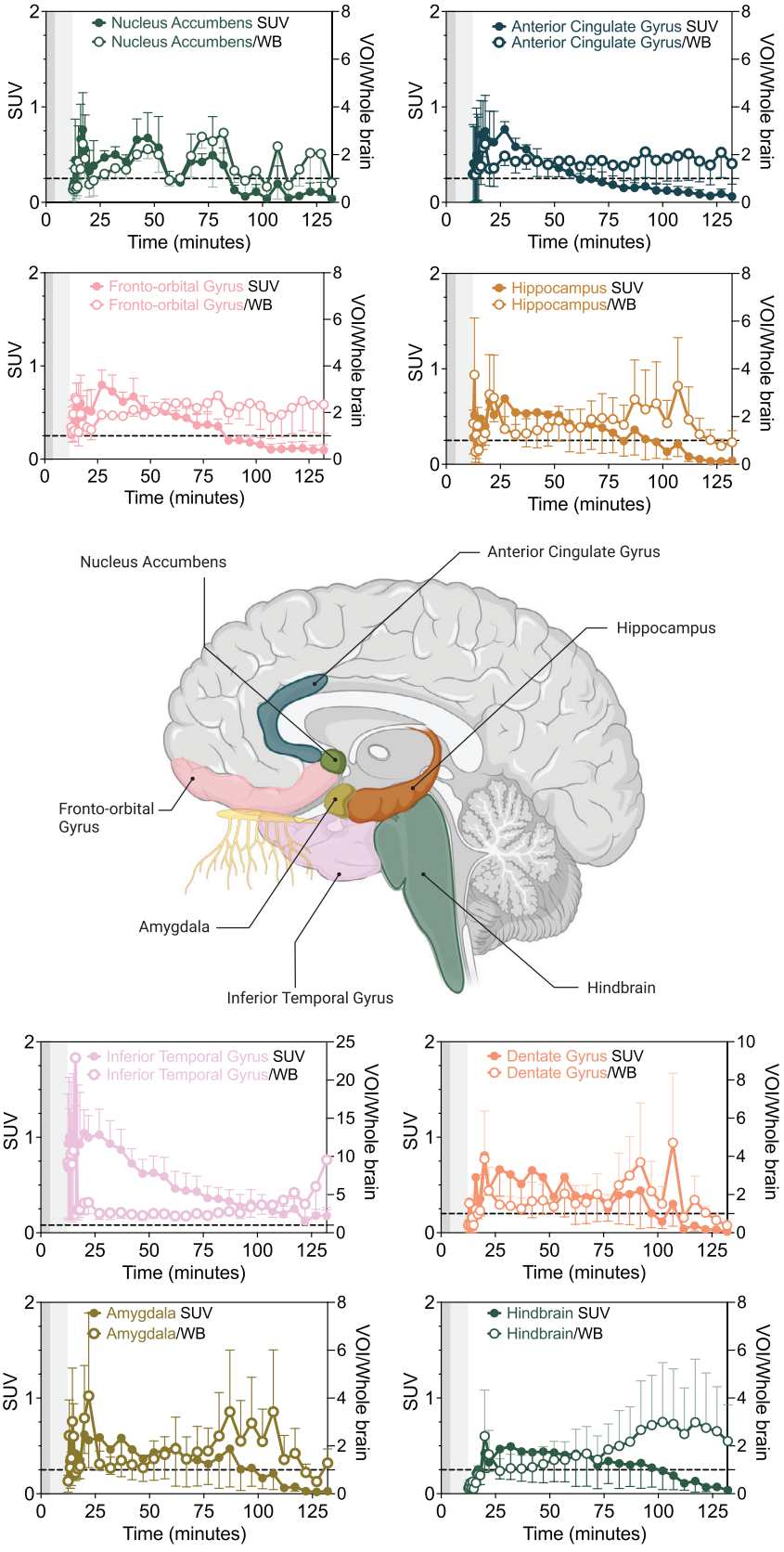

FIGURE 5 Brain regions with the highest [^{18}F]FB-insulin levels show varied kinetics. A human brain illustration highlights atlas subregions with highest AUC values following liquid [^{18}F]FB-insulin instillation by catheter. TACs for the same regions demonstrate changes to regional insulin concentration over time as SUV (solid circles, left axis) and WB normalized SUV (VOI/WB, hollow circles, right axis). For WB normalized SUV (nSUV) TACs, the VOI SUV value was divided by the WB SUV value at the same time point. From top left to bottom right, plots give mean ± standard error (SEM, $n = 3$) for the nucleus accumbens, anterior cingulate gyrus, fronto-orbital gyrus, hippocampus, inferior temporal gyrus, dentate gyrus, amygdala, and hindbrain (does not include cerebellum). Dotted line indicates equivalent activity levels between VOI and WB at VOI/WB = 1 for each graph. Time devoted to dosing or subject transfer to PET scanner are indicated by darker and lighter gray rectangles in plot, respectively. AUC, area under the curve; SEM, standard error of the mean; SUV, standard uptake value; nSUV, whole brain normalized SUV; TAC, time-activity curve; VOI, volume of interest; WB, whole brain.

would increase CSF insulin concentration from 2.50 pM in a moderate/severe AD patient[42] to 71.86 pM, closing the gap between AD and healthy control levels 95-fold. Future studies should aim to pair concurrent [^{18}F]FB-insulin dosing, image acquisition, and sampling from CSF and plasma. Validation of CSF and plasma [^{18}F]FB-insulin concentration estimates, identification of insulin modifications, and refinement of the transfer model and associated insulin kinetics[43] would be important outcomes of such improvements. A refined version of our method may be used to identify CNS insulin levels associated with improved cognitive performance when paired with an interventional study using N2B insulin, which may vary regionally depending on the AD subtype.

Earlier studies demonstrated a relationship between insulin resistance and reduced metabolic activity in the precuneus[44] that was preserved from progression following N2B insulin treatment.[6,22] In contrast, we found that [^{18}F]FB-insulin activity in the precuneus was among the lowest of the brain atlas regions, both over time and acutely (eg, AUC and SUV_{max}) but was present (95% CI 0.00071% to 0.0066% ID, see Figure B.6 of supporting information Appendix B). If our results are representative of the intranasal insulin distribution expected in humans, this may suggest that minor increases in insulin provide protective and/or therapeutic effects. However, unappreciated anatomical differences may exist between humans and cynomolgus macaques that affect distribution to this site and explain the discrepancies between studies. It is also possible that the referenced study sample population had a greater proportion of patients with parietal vulnerability, which was recently highlighted as a distinct pattern of degeneration.[34] The method we've outlined may help to answer such questions related to preferential delivery pathways and treatment responders versus non-responders.

Finally, our results are aligned with reported insulin N2B transfer routes and receptor distribution. Insulin has been shown to travel along olfactory (CN I) and trigeminal (CN V) nerves to reach the CNS,[12,45] which terminate at regions we have identified as having high [^{18}F]FB-insulin availability. CN I travels ventrally and caudally along the fronto-orbital gyrus before diverging to the amygdala and diffusely across the temporal lobe.[33] A recent neuroimaging study found that the anterior cingulate gyrus, fronto-orbital gyrus, inferior temporal gyrus, hippocampus, and amygdala are points of convergence shared by four identified olfactory processing pathways in humans, while a subset of the pathways converge at the caudate (top 10 in SUV_{max}) and the nucleus accumbens.[46] Together, these regions speak to 10 of the 11 regions with the highest AUC, in which the remaining region (hindbrain) is a known projection site of CN V (pons).[16] Additionally, regions with high [^{18}F]FB-insulin availability and long half-lives suggest high binding rates and/or recycling of the radiotracer, which is in agreement with reports of high IR density in the hippocampus, amygdala, and other temporal regions.[47,48] Thus, our results agree with prior studies that implicate olfactory and trigeminal pathways in N2B transfer of insulin. However, connections between the olfactory bulb, fronto-orbital gyrus, and medial temporal lobe were found to be disrupted in AD patients[49] and may reflect structural differences that hinder consistent N2B insulin distribution across patients. Future studies assessing N2B insulin as a prospective intervention may control for such anatomical differences, as failure to do so may yield misleading confounds if distribution along these pathways is impaired.

This work demonstrated the efficacy of a non-invasive and translatable method to track the fate of N2B therapeutics following dosing and is believed to be broadly applicable for the assessment of other therapeutic agents. Application of this technique is likely to have a greater impact if the limitations present in this study are addressed. For example, the small sample sizes limit the statistical conclusions that can be drawn, due in part to high variability in the results. Additionally, without inclusion of CSF, blood, or tissue sampling data, we are unable make claims regarding the state or activity of [^{18}F]FB-insulin in these regions (whether bound, degraded, or recycled) but would like to include such methods in future efforts. Despite the limitations, the results of this study provide impetus to conduct a more detailed investigation into N2B insulin endpoints with larger sample sizes. Ultimately, these methods can be used to identify and optimize prevailing dose formulations, absorption enhancers, and/or delivery approaches to reduce the barriers to efficacious N2B therapeutics in the clinic.

ACKNOWLEDGMENTS

The authors would like to acknowledge the Departments of Radiochemistry and Molecular Imaging at Charles River Laboratories for conducting radiotracer synthesis and imaging, as well as the surgical and animal care staff for their contributions to catheter placement, VOI generation, and subject maintenance and handling. The authors are also grateful to inviCRO for their contributions to image analysis, Drs. Philip Kuehl and Cody Pinger for guidance regarding dosing approaches and 3D printing, and the National Institutes of Health for financial support (grant number R21AG054960). Figures were made using BioRender (Biorender.com) and the scientific color maps batlow and batlowK, which prevent visual distortion of the data and exclusion of readers with color-vision deficiencies.[50]

CONFLICTS OF INTEREST STATEMENT

The authors declare no conflicts of interest.

ORCID

Kylie Smith https://orcid.org/0000-0003-4360-0252

REFERENCES

1. Wickelgren I. Tracking insulin to the mind. *Science*. 1998;280:517-519.
2. Frölich L, Blum-Degen D, Bernstein H-G, et al. Brain insulin and insulin receptors in aging and sporadic Alzheimer's disease. *J Neural Transm*. 1998;105:423-438.
3. Rasgon NL, Kenna HA, Wroolie TE, et al. Insulin resistance and hippocampal volume in women at risk for Alzheimer's disease. *Neurobiol Aging*. 2011;32:1942-1948.
4. Benedict C, Hallschmid M, Schultes B, Born J, Kern W. Intranasal insulin to improve memory function in humans. *Neuroendocrinology*. 2007;86:136-142.
5. Brunner YF, Kofoet A, Benedict C, Freiherr J. Central insulin administration improves odor-cued reactivation of spatial memory in young men. *J Clin Endocrinol Metab*. 2015;100:212-219.

6. Craft S, Baker LD, Montine TJ, et al. Intranasal insulin therapy for Alzheimer disease and amnestic mild cognitive impairment: a pilot clinical trial. *Arch Neurol*. 2012;69:29-38.
7. Reger MA, Watson GS, Green PS, et al. Intranasal insulin administration dose-dependently modulates verbal memory and plasma β-amyloid in memory-impaired older adults. *J Alzheimers Dis*. 2008;13:323-331.
8. Craft S, Newcomer J, Kanne S, et al. Memory improvement following induced hyperinsulinemia in Alzheimer's disease. *Neurobiol Aging*. 1996;17:123-130.
9. Arnold SE, Arvanitakis Z, Macauley-Rambach SL, et al. Brain insulin resistance in type 2 diabetes and Alzheimer disease: concepts and conundrums. *Nat Rev Neurol*. 2018;14:168-181.
10. Pomytkin I, Costa-Nunes JP, Kasatkin V, et al. Insulin receptor in the brain: mechanisms of activation and the role in the CNS pathology and treatment. *CNS Neurosci Ther*. 2018;24:763-774.
11. Jauch-Chara K, Friedrich A, Rezmer M, et al. Intranasal insulin suppresses food intake via enhancement of brain energy levels in humans. *Diabetes*. 2012;61:2261-2268.
12. Lochhead JJ, Kellohen KL, Ronaldson PT, Davis TP. Distribution of insulin in trigeminal nerve and brain after intranasal administration. *Sci Rep*. 2019;9:2621.
13. Lochhead JJ, Wolak DJ, Pizzo ME, Thorne RG. Rapid transport within cerebral perivascular spaces underlies widespread tracer distribution in the brain after intranasal administration. *J Cereb Blood Flow Metab*. 2015;35:371-381.
14. Thorne RG, Pronk GJ, Padmanabhan V, Frey WH II. Delivery of insulin-like growth factor-I to the rat brain and spinal cord along olfactory and trigeminal pathways following intranasal administration. *Neuroscience*. 2004;127:481-496.
15. Thorne RG, Hanson LR, Ross TM, Tung D, Frey WH II. Delivery of interferon-beta to the monkey nervous system following intranasal administration. *Neuroscience*. 2008;152:785-797.
16. Crowe TP, Greenlee MHW, Kanthasamy AG, Hsu WH. Mechanism of intranasal drug delivery directly to the brain. *Life Sci*. 2018;195:44-52.
17. Dhuria SV, Hanson LR, Frey WH II. Intranasal delivery to the central nervous system: mechanisms and experimental considerations. *J Pharm Sci*. 2010;99:1654-1673.
18. Lochhead JJ, Thorne RG. Intranasal delivery of biologics to the central nervous system. *Adv Drug Deliv Rev*. 2012;64:614-628.
19. Villemagne VL, Burnham S, Bourgeat P, et al. Amyloid β deposition, neurodegeneration, and cognitive decline in sporadic Alzheimer's disease: a prospective cohort study. *Lancet Neurol*. 2013;12:357-367.
20. Freeman SM, Samineni S, Allen PC, et al. Plasma and CSF oxytocin levels after intranasal and intravenous oxytocin in awake macaques. *Psychoneuroendocrinology*. 2016;66:185-194.
21. Born J, Lange T, Kern W, McGregor GP, Bickel U, Fehm HL. Sniffing neuropeptides: a transnasal approach to the human brain. *Nat Neurosci*. 2002;5:514-516.
22. Craft S, Claxton A, Baker LD, et al. Effects of regular and long-acting insulin on cognition and Alzheimer's disease biomarkers: a pilot clinical trial. *J Alzheimers Dis*. 2017;57:1325-1334.
23. De Felice FG, Vieira MN, Bomfim TR, et al. Protection of synapses against Alzheimer's-linked toxins: insulin signaling prevents the pathogenic binding of Abeta oligomers. *Proc Natl Acad Sci USA*. 2009;106:1971-1976.
24. Hong M, Lee VM. Insulin and insulin-like growth factor-1 regulate tau phosphorylation in cultured human neurons. *J Biol Chem*. 1997;272:19547-19553.
25. Chapman CD, Schioth HB, Grillo CA, Benedict C. Intranasal insulin in Alzheimer's disease: food for thought. *Neuropharmacology*. 2018;136:196-201.
26. Freiherr J, Hallschmid M, Frey WH II, et al. Intranasal insulin as a treatment for Alzheimer's disease: a review of basic research and clinical evidence. *CNS Drugs*. 2013;27:505-514.
27. Henkin RI. Intranasal insulin: from nose to brain. *Nutrition*. 2010;26:624-633.
28. Jiang Y, Li Y, Liu X. Intranasal delivery: circumventing the iron curtain to treat neurological disorders. *Expert Opin Drug Deliv*. 2015;12:1717-1725.
29. Md S, Bhattmisra SK, Zeeshan F, et al. Nano-carrier enabled drug delivery systems for nose to brain targeting for the treatment of neurodegenerative disorders. *J Drug Delivery Sci Technol*. 2018;43:295-310.
30. Craft S, Raman R, Chow TW, et al. Safety, efficacy, and feasibility of intranasal insulin for the treatment of mild cognitive impairment and Alzheimer disease dementia: a randomized clinical trial. *JAMA Neurol*. 2020;77:1099-1109.
31. George J. Alzheimer's insulin study puzzles researchers. *MedPage Today2019*.
32. Saccone PA, Lindsey AM, Koeppe RA, et al. Intranasal opioid administration in rhesus monkeys: PET imaging and antinociception. *J Pharmacol Exp Ther*. 2016;359:366-373.
33. Allison AC. The secondary olfactory areas in the human brain. *J Anat*. 1954;88:481-488.
34. Levin F, Ferreira D, Lange C, et al. Data-driven FDG-PET subtypes of Alzheimer's disease-related neurodegeneration. *Alzheimers Res Ther*. 2021;13:49.
35. Braak H, Braak E. Neuropathological stageing of Alzheimer-related changes. *Acta Neuropathol*. 1991;82:239-259.
36. Karageorgiou E, Miller BL. Frontotemporal lobar degeneration: a clinical approach. *Semin Neurol*. 2014;34:189-201.
37. Sanderson TH, Kumar R, Murariu-Dobrin AC, Page AB, Krause GS, Sullivan JM. Insulin activates the PI3K-Akt survival pathway in vulnerable neurons following global brain ischemia. *Neurol Res*. 2009;31:947-958.
38. Van Laere K, Vanhee A, Verschueren J, et al. Value of 18fluorodeoxyglucose-positron-emission tomography in amyotrophic lateral sclerosis: a prospective study. *JAMA Neurol*. 2014;71:553-561.
39. Verger A, Barthel H, Tolboom N, et al. 2-[(18)F]-FDG PET for imaging brain involvement in patients with long COVID: perspective of the EANM Neuroimaging Committee. *Eur J Nucl Med Mol Imaging*. 2022;49:3599-3606.
40. Buciuc M, Botha H, Murray ME, et al. Utility of FDG-PET in diagnosis of Alzheimer-related TDP-43 proteinopathy. *Neurology*. 2020;95:e23-e34.
41. Gray SM, Meijer RI, Barrett EJ. Insulin regulates brain function, but how does it get there? *Diabetes*. 2014;63:3992-3997.
42. Craft S, Peskind E, Schwartz MW, Schellenberg GD, Raskind M, Porte D. Cerebrospinal fluid and plasma insulin levels in Alzheimer's Disease. *Neurology*. 1998;50:164-168.
43. Taubel JC, Nelson NR, Bansal A, et al. Design, synthesis, and preliminary evaluation of [(68)Ga]Ga-NOTA-insulin as a PET probe in an Alzheimer's disease mouse model. *Bioconjug Chem*. 2022;33:892-906.
44. Baker LD, Cross DJ, Minoshima S, Belongia D, Watson GS, Craft S. Insulin resistance and Alzheimer-like reductions in regional cerebral glucose metabolism for cognitively normal adults with prediabetes or early type 2 diabetes. *Arch Neurol*. 2011;68:51-57.
45. Fan LW, Carter K, Bhatt A, Pang Y. Rapid transport of insulin to the brain following intranasal administration in rats. *Neural Regen Res*. 2019;14:1046-1051.
46. Zhou G, Lane G, Cooper SL, Kahnt T, Zelano C. Characterizing functional pathways of the human olfactory system. *eLife*. 2019;8:e47177.
47. Unger JW, Livingston JN, Moss AM. Insulin receptors in the central nervous system: Localization, signalling mechanisms, and functional aspects. *Prog Neurobiol*. 1991;35:343-362.
48. Gollapelli K, Damuka N, Bansode A, et al. Preliminary evaluations of [68Ga]-NOTA-insulin in animal models of Alzheimer's disease. *J Nucl Med*. 2023;64:P1228.

49. Zou YM, Lu D, Liu LP, Zhang HH, Zhou YY. Olfactory dysfunction in Alzheimer's disease. *Neuropsychiatr Dis Treat*. 2016;12:869-875.
50. Crameri F, Shephard GE, Heron PJ. The misuse of colour in science communication. *Nat Commun*. 2020;11:5444.

SUPPORTING INFORMATION

Additional supporting information can be found online in the Supporting Information section at the end of this article.

How to cite this article: Smith K, Fan J, Marriner GA, Gerdes J, Kessler R, Zinn KR. Distribution of insulin in primate brain following nose-to-brain transport. *Alzheimer's Dement*. 2024;10:e12459. https://doi.org/10.1002/trc2.12459